Hindawi
International Transactions on Electrical Energy Systems
Volume 2022, Article ID 2934167, 11 pages
https://doi.org/10.1155/2022/2934167

Research Article

Design and Implementation of Hybrid PV/Battery-Based Improved Single-Ended Primary-Inductor Converter-Fed Hybrid Electric Vehicle

Belqasem Aljafari,[1] **Gunapriya Devarajan**,[2] **Selvi Arumugam**,[3] **and Indragandhi Vairavasundaram**[4]

[1]*Department of Electrical Engineering, College of Engineering, Najran University, Najran 11001, Saudi Arabia*
[2]*Department of Electrical and Electronics Engineering, Sri Eshwar College of Engineering, Coimbatore 641 202, India*
[3]*Department of Computer Science and Engineering, M.Kumarasamy College of Engineering, Karur 639 113, India*
[4]*School of Electrical Engineering, Vellore Institute of Technology, Vellore 632 014, India*

Correspondence should be addressed to Gunapriya Devarajan; gunapriyadevarajan@gmail.com

Received 8 May 2022; Accepted 23 July 2022; Published 28 August 2022

Academic Editor: Faroque Azam

In order to enhance the power transformation stage's power transfer capabilities and efficiency, in this article, improved three-port two step-up single-ended primary-inductor converters (SEPIC) converter fed (Photovoltaic)PV- Hybrid Electric Vehicle was proposed. In comparison to the standard single-stage SEPIC, the proposed converter accepts a wider range of input voltages. The proposed three-port converter uses a multiple-winding high-frequency transformer (HFT) to integrate the dual sources and provide greater voltage gain with lesser elements. Furthermore, by predicting the drive torque need, the power management algorithm (PMA) included with the proposed PV-hybrid electric vehicle (HEV) minimizes the drive motor's power consumption. An experimental model with a power output of 6 kW and a voltage range of 12 to 600 volts has been created and tested. The designed model has 94.11% efficiency.

1. Introduction

In recent years, there has been an enormous growth in efforts to improve, establish, and manage renewable energy sources (RESs). These can be affected by a combination of reasons. Conventional energy sources (fossil fuels) are known to pollute and degrade the environment as well as contribute to global warming and the greenhouse effect. The utilization of RES for electricity generation has become unavoidable due to the need to reduce carbon emissions. In the transportation industry, conventional automobiles also contribute to environmental pollution and greenhouse gas emissions. When these vehicles burn gasoline, coal, or natural gas, they emit hazardous combustion components such as nitrogen oxides, sulphur dioxide (SO2), and carbon dioxide (CO2). According to environmental data providers in the United States [1], the transport industry accounts for about a quarter of all greenhouse gas (GHG) emissions, as presented in Figure 1. Internal combustion engine (ICE) vehicles lose energy along with heat loss and friction on the moving segment, as seen in [2]. With the ICE being phased out, electric vehicles (EVs) become the greatest possibility for lowering outflow [3]. Battery EVs require a big battery with a restricted span for propulsion [4]. The HEV has emerged as a viable option for decreasing transportation-related GHG emissions, with the use of a variety of energy sources targeted to reduce vehicle running costs and enhance efficiency. HEVs are expected to be more fuel-efficient than ICE vehicles and to maintain their state of charge (SOC) during the journey [5]. Completely green charging systems (CGCSs) reduce CO2 emissions by charging EVs using renewable energy, hence encouraging the adoption of

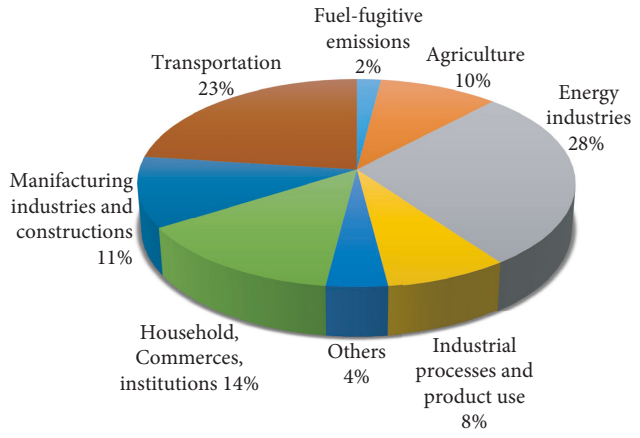

Figure 1: Greenhouse gas emissions by industry in 2018 [1] according to the Intergovernmental Panel on Climate Change.

renewable energy sources in the energy sector. EVs are charged from the grid, yet in practice, EVs do not consume coal but rather renewable energy.

1.1. Motivation. The main problems with HEVs are regenerative braking and the fuel tank. Plug-in hybrid electric vehicles (PHEVs) with externally charged battery packs were developed to overcome this problem [6]. Among other renewable energy systems, PV frameworks have seen the most progress and construction in recent years. The majority of the PV framework development that is released as an off-grid market is intended for the grid-connected PV industry. A grid-connected PV infrastructure is described in [7]. A DC converter is necessary for the front-large step-up to optimize and control PV voltage at the DC bus voltage (400 or 800 V). The output voltage of a PV model is often lower (20–50 V). The common-mode current in a grounded PV system is ignored by a mechanism. It includes features that are of interest, such as high voltage, low recovery of leakage energy, and low switch stress; moreover, the converter has more source ripple current, and it contributes to the PV segment's maximum power point tracking (MPPT). In [8] a high-voltage gain with input current ripple cancellation techniques has been discussed. According to the regular driving cycle, a large number of PV-powered EVs have been developed. PV power generating systems, as compared to other types of power generation, provide more benefits by supplying clean and abundant energy [9, 10].

The torque from the engine and motor is distributed to the driving shaft using a PMA based on vehicle dynamics [11]. It aids in improving EV energy efficiency. To increase the efficiency of the DC/AC converter, Battiston et al. [12] presented an enhanced flatness control technique for a quasi-Z-source inverter-fed permanent magnet synchronous motor-operated EV. The flatness controller has a great dynamic performance and is stable. A review of the AC/DC-DC power converter for EV has been discussed [13]. The adoption of maximum step-up converters with higher efficiency and reliability for transforming infinite energies into the power grid will be substantially catalyzed by the expansion of RES [14]. Vehicle to grid (V2G) capability is provided by PHEVs, which solves the problem of restricted driving range [15]. A hybrid energy source system for EV is an integration of a battery and super capacitor that improves overall efficiency and battery lifespan [16–20].

The authors in [21, 22] described a three-port converter for high power applications that integrates the battery and PV. In particular, coupled inductors (CIs) with high turn ratios create leak inductance due to voltage spikes beyond the switches, as well as greater power losses, which diminish efficiency. This issue could be answered by healing energy from the leakage inductor. The use of a voltage clamp circuit in CI converters can result in an outstanding performance [23]. The three-port converter's CI contributes to achieving high-voltage gain. It facilitates in lowering of voltage stress across the switch. By reprocessing the energy held in the leakage inductors, the active clamp circuit enhances the power conversion efficiency. In [24], a comparison of the two and three-level inverter-fed EVs was given. In addition, an innovative control strategy for balancing the three-level inverter's DC link capacitors is described, which reduces the switching sequences as different from traditional pulse width modulation (PWM) strategies.

The voltage balancing method lowers total inverter switching losses and eliminates voltage distortion. The PV interfaced HEVs (PV-HEVs) are considered to be a step ahead in transport and are able to replace ICE-based conventional vehicles. To avoid the use of new balancing circuits, a new vitality control system must be developed to observe the vehicle-to-home (V2H) and home-to-vehicle (H2V) abilities. When the drive attaches the PV-HEV to the home, a controller based on the fuzzy logic controller (FLC), which combines the SOC, has been proposed to minimize the SOC. Faraji and Farzanehfard [25] presented a non-isolated large step-up three-port converter that is meant to provide two distinct power flow routes from each source. To enhance gain and remove the leaking inductance, the CI approach was utilized. The active clamp circuit used with the given architecture provides zero voltage switching (ZVS), which reduces the switching losses and stress [26]. Bharathidasan et al. [27] described a multi-input DC-DC converter using CI. Gules et al. [28] elaborated a brushless DC (BLDC) motor drive fed by a conventional low step-up SEPIC designed for EV applications. It uses a parallel LC resonant tank circuit to combine a soft-switching approach and a CI [29]. Due to its easy architecture and ease of accomplishment of soft switching, a bidirectional converter designed using a phase shift control technique is usually processed for HEV. Previous to the insulated gate bipolar transistor (IGBT) being ON, a steady offset current of the inductor is carried on to forward bias the anti-parallel diodes and achieve ZVS. In order to reduce ripple on the source and load postern, a novel multi-port ZVS converter was proposed in [30]. It may also connect three different voltage sources with the help of multiple switches. To decrease ripple and diminish the average current flowing continuously in the semiconductor devices, Saadatizadeh et al. [31] proposed

a high-voltage conversion ratio interleaved boost converter with low voltage stresses on diodes and switches.

The interleaved topology, which incorporates diode-capacitor modules, helps to boost gain and diminish stress on the switch. A CI-based non-isolated DC-DC converter with strong boosting gain has been proposed in [32]. A coupled inductor-based multi-input DC-DC converter is presented in [33]. The use of a three-winding CI results in a large gain and aids in minimizing switching stress. The SEPIC-based DC-DC converter is also found to have more advantages than traditional DC-DC converters [34, 35]. Figure 2 shows a conventional single step-up SEPIC without the CI utilized to transmit energy from a PV. In the proposed topology, energy transfer ability and voltage gain are enhanced using a three-port two, step-up SEPIC converter by integrating PV array and battery. The enhanced SEPIC's topology is derived from the SEPIC's single-stage boosting design.

The fundamental single step-up SEPIC without a CI has a gain that is nearly double that of a classical step-up converter and a switching voltage that is half that of a traditional step-up converter. The improved SEPIC boosts the gain by using a three-winding CI as a flyback transformer, and the main benefits are validated. The converter technique is proposed in Section 2, design considerations are given in Section 3, control strategy is given in Section 4, power flow management algorithm is given in Section 5, results and discussion are given in Section 6, and Section 7 gives the conclusions.

2. Proposed Converter

. The architecture of the proposed three-port two-step-up SEPIC converter-driven PV interconnected to HEV is shown in Figure 3 The PV and battery provide the PV-HEV with its electricity. The HEV is more efficient than a traditional EV in this approach. The battery and ICE in a standard HEV add to the vehicle's weight, lowering its efficiency. When compared to the ICE integrated model, the proposed structure is constructed exclusively with BLDC motor drive, resulting in lower system weight. The designed PV-HEV has the benefit of accepting a broad range of input voltage and stabilizing the VSI DC link voltage to improve the drive motor's performance.

. The major concern of the improved three-port two-step-up SEPIC converters is to enhance the voltage gain. A three-winding linear transformer is added between the source and the VSI to modify the standard SEPIC. Add on one extra circuitry in a back-to-back connection; a standard SEPIC becomes a three-port SEPIC. Figure 4 shows the power circuit, which consist of a battery, PV, an improved three-port two boosting SEPIC connection with voltage doubler rectifier, three phases VSI, and a BLDC motor with driving lines. To make the theoretical analysis simple, the battery and PV are used as a source, with the semiconductors treated as independent elements. To demonstrate the theoretical analysis of the system, improved three-port two-step-up SEPIC converter-driven PV-HEV operating in six distinct modes are described in this section.

Mode 1. During subinterval [t_0-t_1], the battery and PV array will continue to charge L_1, L_2, and L_3, as seen in Figure 5(a). The voltage stored in the C_2 and C_3 is discharging to the HFT until t_1. The diodes D_1 and D_2 are reverse biased, with the higher diode voltage equal to the sum of the voltages across C_1 and C_2 or C_3 and C_4. Equations (1) and (2) show the voltage equations of L_1, L_2, and L_3. The VSI's power switches S5, S6, and S1 are all on, providing the BLDC motor drive with a controlled AC voltage.

$$V_{L1} = V_{L3} = V_{pv}, \tag{1}$$

$$V_{L2} = V_b, \tag{2}$$

where V_{L1} is inductor 1 voltage, V_{L2} is inductor 2 voltage, V_{L3} is inductor 3 voltage, V_b is the battery voltage, and V_{pv} is the PV voltage.

Mode 2. In [t_1-t_2], the inductors L_1, L_2, and L_3 are entirely demagnetized by the SEPIC's Q_1, Q_2, and Q_3. The PV array output voltage charges L_3 at the end of this subinterval. D_1 is forward biased, allowing L_1 to transfer its stored energy to C_2. Figures 5(b) and 6 show the analogous circuit for this subinterval as well as the relevant operating waveforms. In equations (3)–(5), the battery's voltage equations, C_2 and C_3, are described.

$$V_b = \frac{V_{pv}}{1 - D_{Q3}}, \tag{3}$$

$$V_{C2} = \frac{V_{pv}}{1 - D_{Q1}}, \tag{4}$$

$$V_{C4} = \frac{V_{pv}}{1 - D_{Q2}}, \tag{5}$$

where V_{C2} is capacitor 2 voltage, D_{Q1}, D_{Q2}, and D_{Q3} are the duty ratios of Q_1, Q_2, and Q_3, and V_{C4} is capacitor 4 voltage.

Mode 3. In [t_2-t_3], Q_1 is turned on, while Q_2 and Q_3 are turned off. Figures 5(c) and 6 show the analogous circuit for this subinterval as well as the important operating waveform. The energy transformer from the primary to secondary of the HFT exists until the mode ends or the switches are turned back on. The VSI's power switches S_6, S_1, and S_2 are used to provide a managed AC voltage in time with the Hall effect sensor output. The power transfer to the capacitors C_2 and C_4 is completed, and the diodes D_1 and D_2 are turned off.

Mode 4. Figures 5(d) and 6 show the subinterval's corresponding circuit and essential operating waveforms. The current of diodes D_1 and D_2 is continuously lowered when the converter power switches Q_1 and Q_2 are ON at t_3. After switching the converter power switch Q_3 to OFF, the potential polarity across L_3's forward bias D_3 is reversed, and the battery is charged as of subinterval 2. Power is transferred from the DC link to the BLDC motor using power IGBTs S_1, S_2, and S_3.

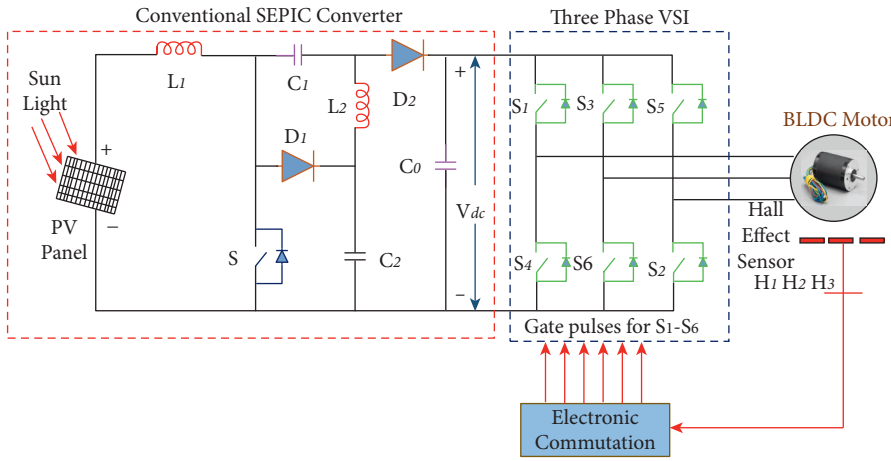

Figure 2: Conventional low step-up SEPIC without a magnetizing inductor.

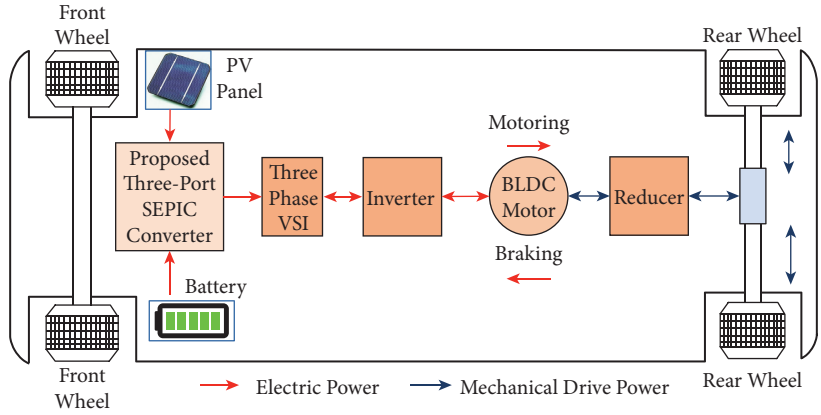

Figure 3: The proposed PV-interconnected hybrid EV's system architecture.

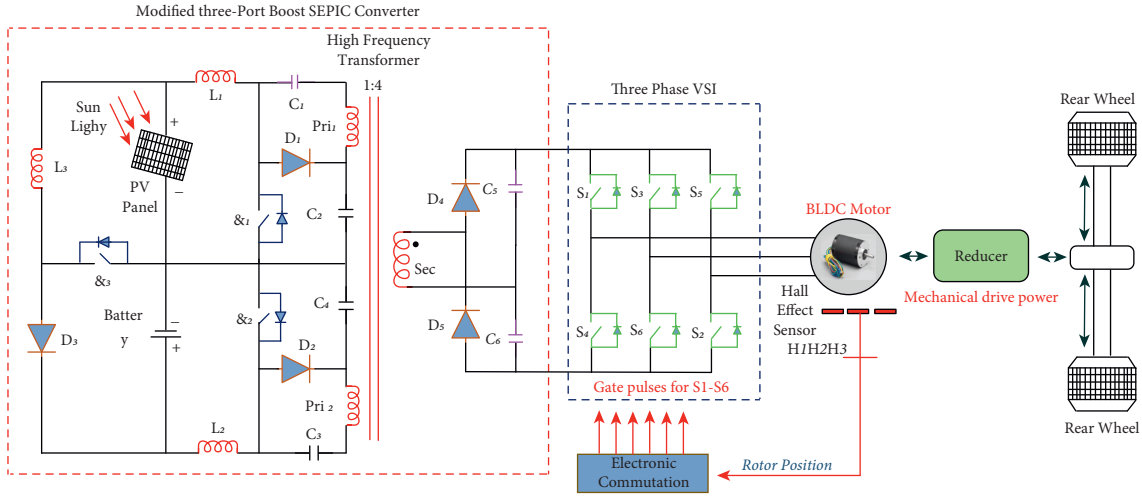

Figure 4: The improved three-port, two step-up SEPIC converter fed PV-HEV configuration.

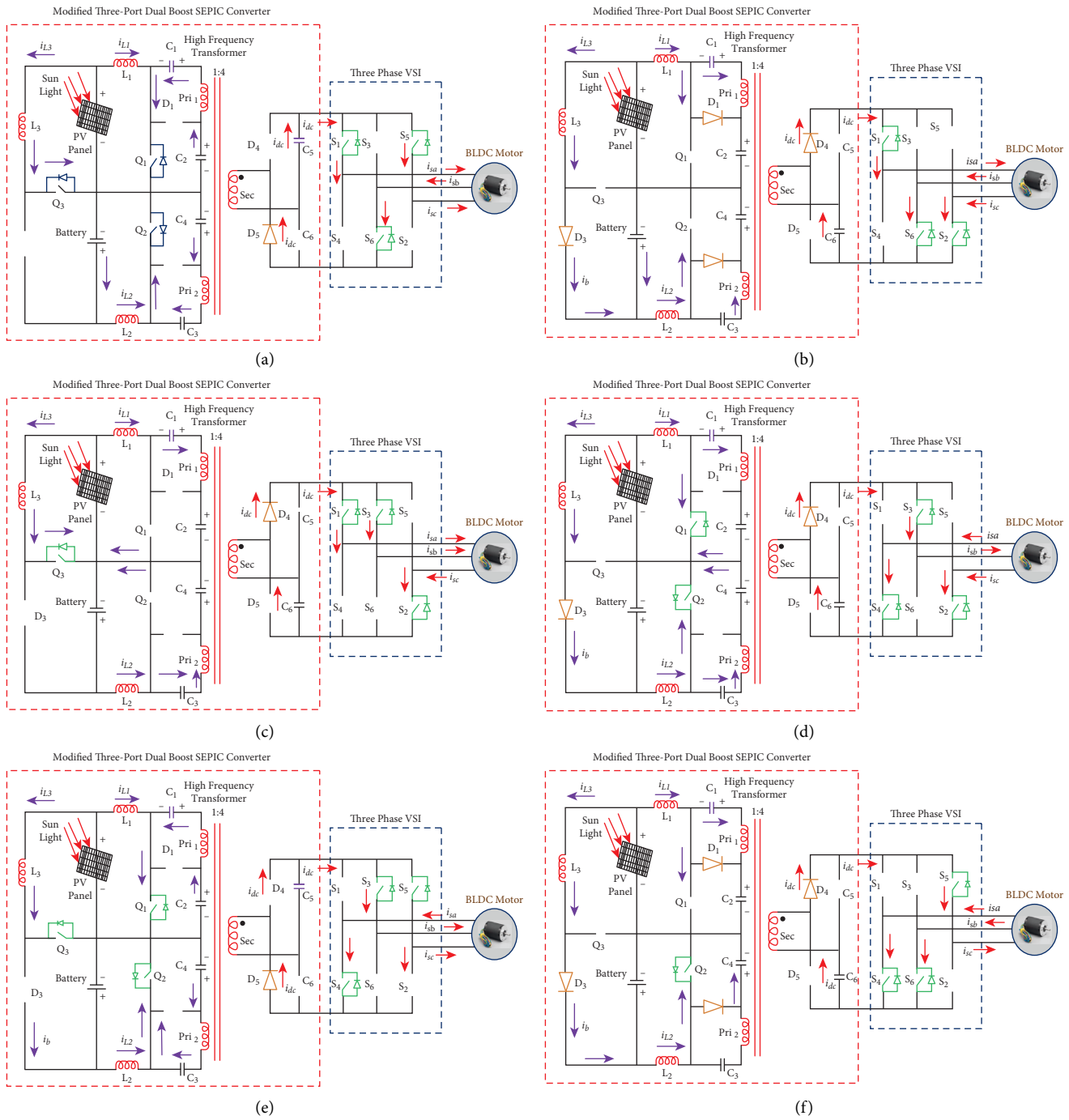

Figure 5: The proposed converter has several switching modes.

Mode 5. The voltage control approach generates a pulse that activates Q_1, Q_2, and Q_3 during this subinterval. The power produced by the PV is stored by the input inductors L_1, L_2, and L_3 in a manner similar to mode 1. The primaries of the HFT receive C2 and C4 during this subinterval. D_1 and D_2 are backward biased diodes. S_2, S_3, and S_4 IGBTs are all on as shown in Figures 5(e) and 6.

Mode 6. The switching states and current flow channel of the sixth mode of operation are shown in Figures 5(f) and 6. This mode begins at time t_5 and ends at time t_6. To discharge the energy stored in the inductors L_1, L_2, and L_3, the IGBTs of the dual step-up SEPIC Q_1, Q_2, and Q_3 are turned off. PV and L_3 work together to charge the battery bank. D_1 conducts current from L_1 to C_2 during this subinterval. Meanwhile, D_2 discharged L_2 to zero.

The voltage across the power switches and diodes is lesser than the SEPIC's output voltage. The presence of a high-frequency isolation transformer limits the diode's di/dt. The HFT boosting ratio is chosen so that the SEPIC has a

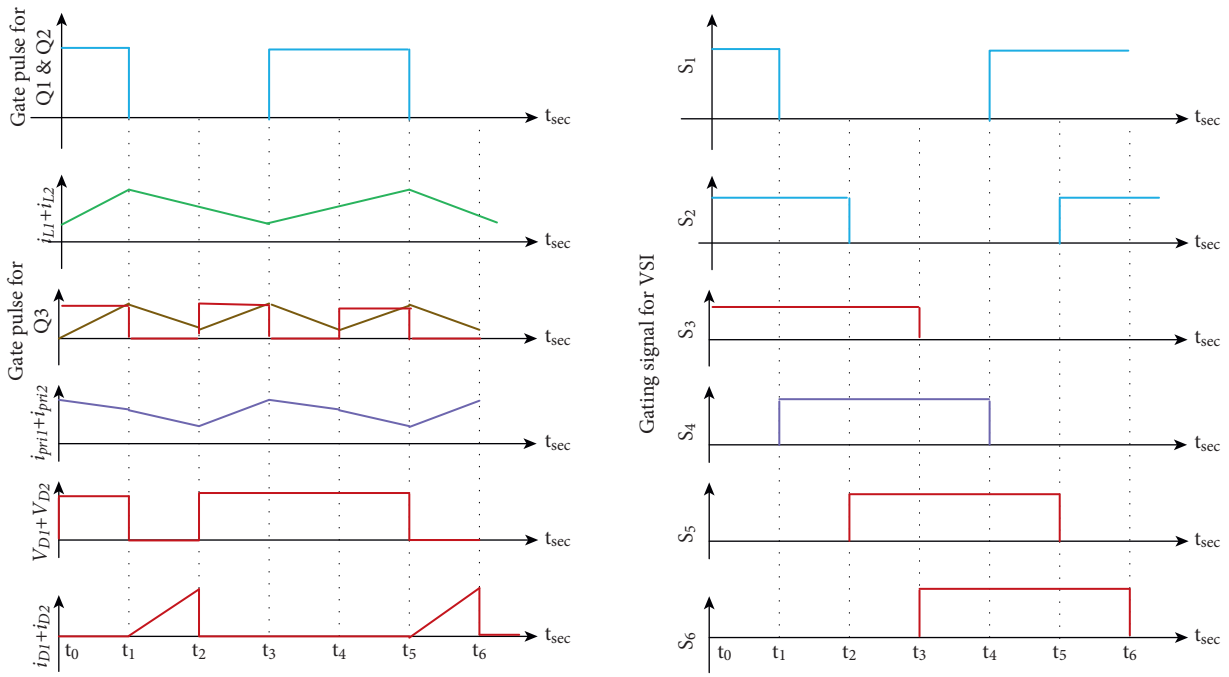

Figure 6: Switching patterns of the proposed converter.

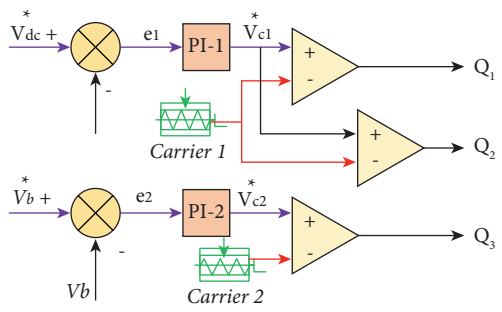

Figure 7: The proposed converter's control strategy.

strong boosting gain over a wide variety of inputs. The proposed three-port SEPIC's theoretical current and voltage waveforms are shown in Figure 6. Consider equation (6) to get the greater gain of the improved three-port SEPIC with HFT and voltage doubler rectifier. The modified SEPIC's boosting factor is enhanced by adding the HFT turn ratio without affecting the inductor or switch ratings.

$$V_{dc} = \left(\frac{V_{pv}}{1 - D_{Q1}} + \frac{V_b}{1 - D_{Q2}}\right) * (1 + n). \tag{6}$$

The three-winding HFT turn ratio can be stated as follows.

$$n = \frac{N_{Ls}}{N_{Lp1} + N_{Lp2}}, \tag{7}$$

where n is the turn ratio of HFT, V_{dc} is the DC link voltage, N_{Ls} is the no. of turns in secondary of HFT, N_{Lp1} is the no. of turns in primary 1, and N_{Lp2} is the no. of turns in primary 2 of HFT.

3. Design Considerations

3.1. Inductor Design. The voltage equations described in equations (1)–(6) and the current flowing through a specific aspect are being utilized to determine the inductor value and capacitor utilized in DC-DC converters. The inductor's stored energy is calculated using the inductor and the current flowing through the component, as shown in

$$W = \frac{1}{2}LI^2. \tag{8}$$

The storage capacity of the inductor is determined by the inductor (L) size and core. The magnetic field density, B, can be written as

$$B = \mu_0\mu_r \cdot H. \tag{9}$$

The inductor's field energy may be calculated using

$$W = \frac{1}{2}\int \vec{H}\vec{B}dv. \tag{10}$$

The inductor's stored energy is exactly proportional to the air gap volume in an air-cored inductor. Equation (11) can be utilized to determine the lower volume (V) of the air gap necessary for the inductor.

$$V \geq \frac{LI^2\mu_0}{B_{\max}^2}. \tag{11}$$

The magnetic conductance is used to compute the number of turns in the inductor, as shown in

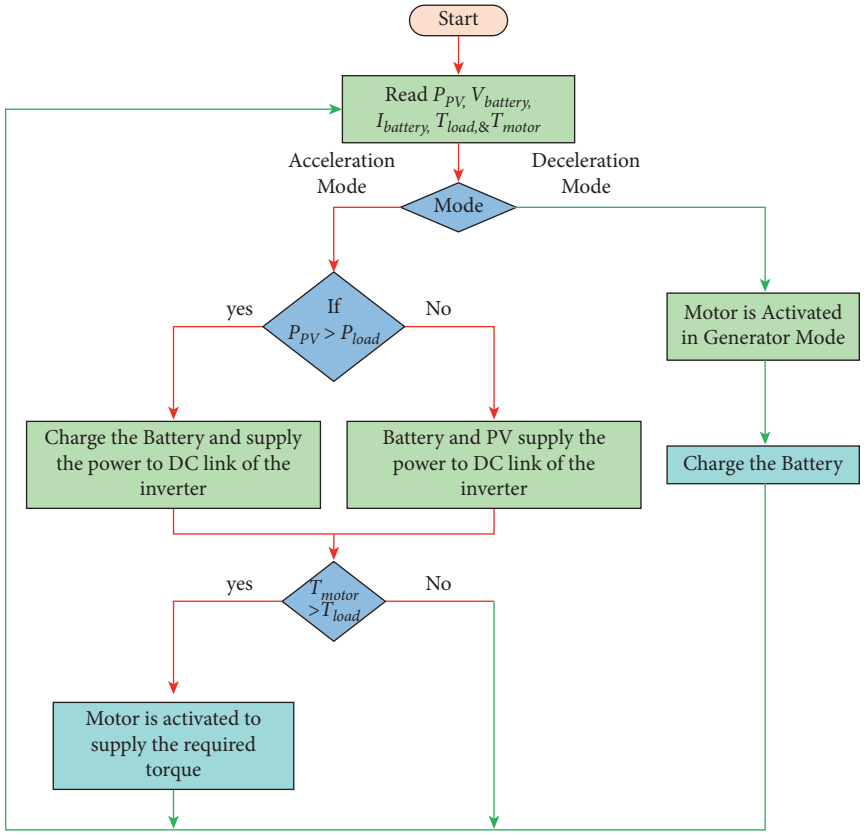

Figure 8: Power flow management algorithm flowchart.

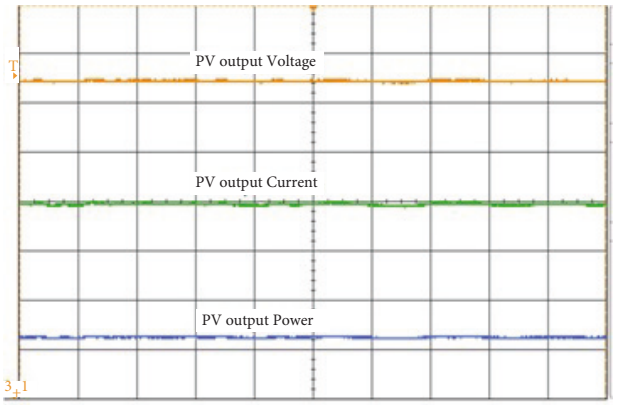

Figure 9: PV output voltage, current, and power.

$$N = \sqrt{\frac{L}{A_L}}, \tag{12}$$

where L is the inductor, I is the current, B is the flux density, B_{max} is the maximum flux density, A_L is the magnetic conductance, μ_r is the relative permeability, μ_0 is the absolute permeability, W is the energy stored in the inductor, and H is the flux intensity.

3.2. Design of HFT. The proposed system's HFT operates at a frequency of 25 kHz. It may also increase the input voltage to four times its original value. The transformer's size is determined by the operating frequency and the transformer's kilovolt-ampere rating. The HFT decreases in size as the switching frequency increases. The HFT's primary and secondary currents are as follows:

$$I_{\text{pri}} = \frac{KVA}{V_{\text{pri}}},$$
$$I_{\text{sec}} = \frac{KVA}{V_{\text{sec}}}. \tag{13}$$

The primary and secondary voltages of HFT are expressed according to Faraday's law of electromagnetic induction.

$$V_{\text{pri}} = N_{\text{pri}}\frac{d\varphi}{dt},$$
$$V_{\text{sec}} = N_{\text{sec}}\frac{d\varphi}{dt}. \tag{14}$$

For both primary and secondary HFT, the minimum number of turns necessary is stated as

$$N_{\text{pri\_min}} = \frac{V_{\text{pri}} \cdot T/2}{\Delta B \cdot A_{\text{min}}},$$
$$N_{\text{sec\_min}} = \frac{V_{\text{sec}} \cdot T/2}{\Delta B \cdot A_{\text{min}}}, \tag{15}$$

Table 1: Comparison between the proposed and conventional SEPICs.

V_{pv} and V_b in V	Duty cycle (D) in %	Conventional SEPIC				Improved SEPIC			
		Voltage gain			Efficiency (%)	Voltage gain			Efficiency (%)
		$n=1$	$n=2$	$n=3$		$n=1$	$n=2$	$n=3$	
12	20	2.50	3.75	5	92.14	5	7.50	10	93.52
	40	3.33	5	6.67	92.16	6.67	10	13.33	94.11
	60	5	7.50	10	92.36	10	15	20	93.92
	80	10	15	20	92.60	20	30	40	93.76
	90	20	30	40	92.80	40	60	80	92.98

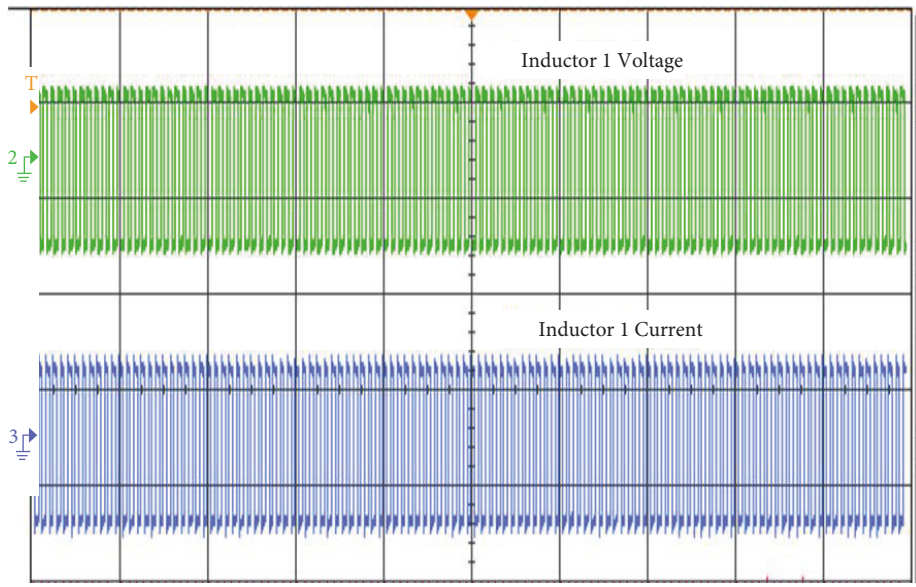

Figure 10: Inductor 1 voltage and current.

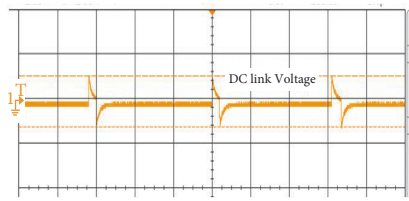

Figure 11: DC link voltage.

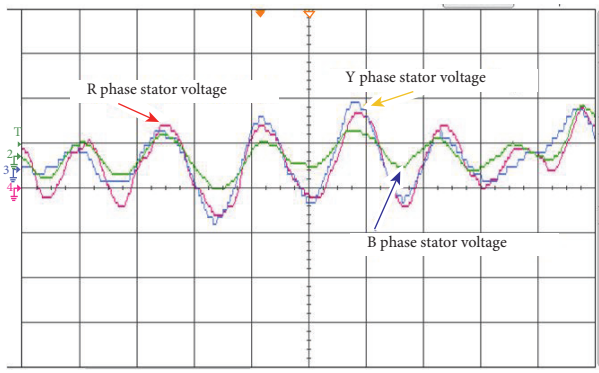

Figure 12: Three-phase stator voltage.

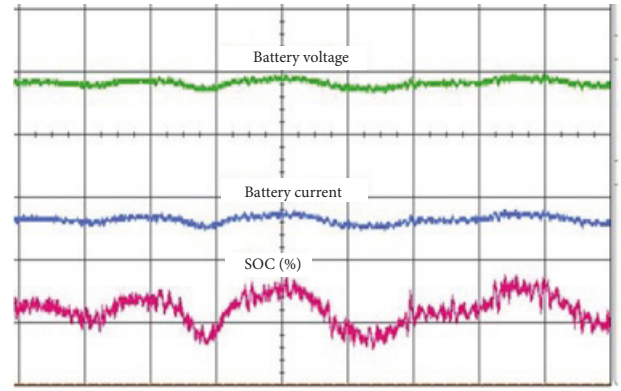

Figure 13: Battery voltage, current, and SOC (%).

where N_{pri} represents turns in primary, N_{sec} represents turns in secondary, T is the total time period, A_{min} is the minimum area of the core, and ΔB is the change in flux density.

4. Control Strategy

To create the gating pulses for switching Q_1, Q_2, and Q_3 in the proposed work-employed HEV, dual voltage control loops are used. The VSI's DC link voltage (Vdc) is

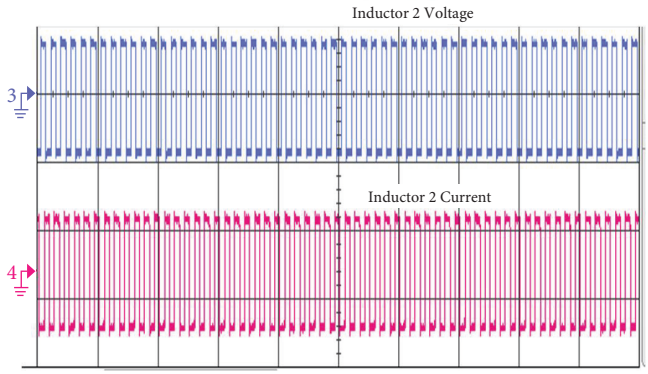

Figure 14: Inductor 2 voltage and current.

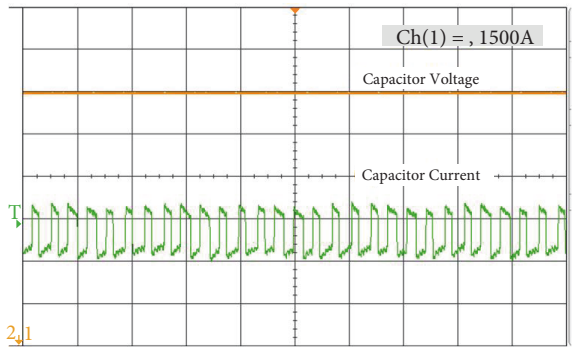

Figure 15: Output capacitor voltage and current.

controlled by gate pulses generated by the power switches Q_1 and Q_2. When a large change in the converter's input voltage is obtained, it aids in regulating the HEV's DC link voltage. As shown in Figure 7, the proposed system's control method is comprised of two PI voltage control loops. The voltage control loop1 developed with the PI controller 1 regulates the duty ratio of Q1 and Q2 to improve the PV voltage and maintain the DC link voltage. To manage the PV output voltage, voltage control loop 2 developed with the PI controller 2 regulates the duty ratio of Q_2. The SEPIC boosting gain is determined by the HFT's turn ratio. By subtracting Vdc∗ and Vdc, as shown in equation (16), the error signal e1 is obtained. As shown in equation (17), the error signal e2 is derived by subtracting Vb∗ and Vb.

$$e_1 = V_{dc}^* - V_{dc}, \tag{16}$$

$$e_2 = V_b^* - V_b, \tag{17}$$

where V_{dc} is the actual DC link voltage and $V_{dc}*$ is the reference DC link voltage.

Two independent PI controllers process the error signals e_1 and e_2 to generate the SEPIC converters needed to control signals. The duty cycle of the power switches Q_1, Q_2, and Q_3

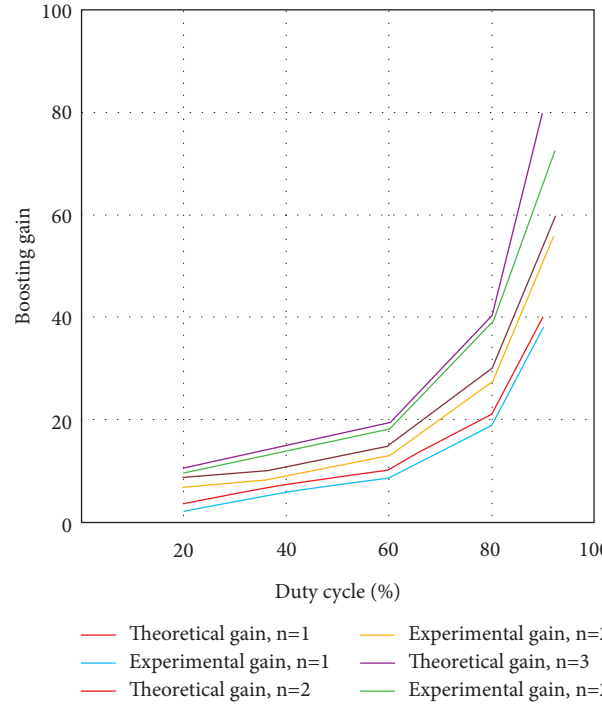

Figure 16: Comparison of theoretical and experimental results.

is determined by the amount of the control signals Vc1∗ and Vc2∗.

5. Power Flow Management Algorithm

A power management algorithm (PMA) is required to control the power stream between the source and the load in the proposed PV-HEV, which consists of power-producing sources (PV, battery bank, and BLDC motor). The power stream connecting the output voltage and motor drive is controlled using the estimated load torque demand. The PMA included in the proposed PV-HEV improves the efficiency and operating time of the HEV. The battery and PV, which are combined with the converters, provide the necessary power to the motor in order for them to provide the torque required by the load. When surplus power generation in the PV is identified, the proposed work is set to step up operation to transmit power from the PV to the DC-link.

The proposed converter, when operated in boost mode, transmits the DC-power links to the battery. Drive motors must be deactivated when $I_{battery\text{-}max}$ arrives. The drive's power balancing is given in

$$V_{pv}I_{pv} = V_{battery}I_{battery} + V_{BLDC}I_{BLDC}. \tag{18}$$

The BLDC motor converts the kinetic energy in the driveline into electrical energy in regenerative braking mode. The AC voltage produced by the BLDC motors is rectified by power diodes coupled in shunt with the inverter's IGBTs. The rectified DC voltage is transferred to the battery unit by the proposed converter when it is enabled in boost

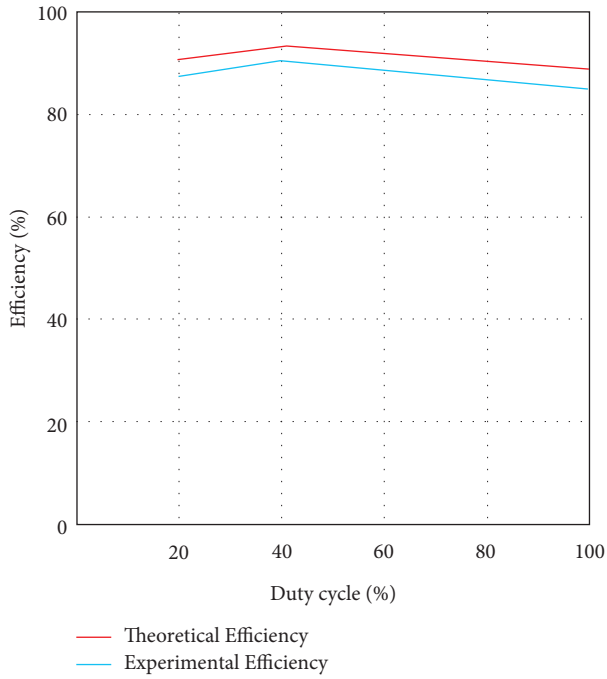

Figure 17: The efficiency of the proposed converter.

operation. Figure 8 shows the algorithm for controlling the power flow.

6. Results and Discussion

12-volt batteries were used to create the experimental model. The converter's switching frequency was 25 kHz. The XC161 microcontroller was used to execute the proposed system's control approach and sense the BLDC motor's rotor position. The XC161 microcontroller is used to produce the appropriate firing pulse for the converter, and VSI is used to manage the BLDC motor speed. The microcontroller's PWM approach creates the need for a pulse for the three phases of VSI in synchrony with the drive motor's rotor position. The program was downloaded to the 16 bit XC161 microcontroller with the KEIL-ULINK kit. The signal conditioning board receives the measured voltage across the VSI's output voltage and converts it to a form that can be measured. The experimental results were achieved using the proposed configuration in a real-time setting. Figures 9–15 show the results of the proposed converter-fed PV-HEV prototype model. The contrast is summed up in Table 1.

The proposed converter has a greater voltage conversion ratio than the traditional SEPICs in the literature, according to the statistical study. The theoretical and experimental findings of the proposed converter are compared in Figure 16. The drive system's efficiency is 94.11%, and Figure 17 shows the voltage and current stress on the converter's major switches. Furthermore, the proposed converter's efficiency is unaffected by changes in PV array voltage or load torque. As a result, the suggested converter is ideal for HEV applications. A minimal voltage PV array/battery can be interfaced with a large voltage DC-link using the proposed PV-HEV modified SEPIC.

7. Conclusion

. This paper presents an improved three-port two-step-up SEPIC converter fed PV-HEV to enhance voltage gain. The isolation in the middle of the PV system and driving unit is provided by the SEPIC with HFT. Furthermore, it supplies two phases of increasing the PV voltage and assists in increasing the gain of the traditional SEPIC. The static gain of the power circuit with HFT and voltage doubler rectifier is double that of a traditional SEPIC. The proposed converter's efficiency is calculated to be 94.1%. Experiments have presented that the proposed converter is effective in enhancing a higher range of input voltages. The main advantage of proposed converter circuit is that it has a greater gain for a given duty cycle. In future scope, this topology can also be applied in the various applications which require reduced losses, high power density, and low weight and volume. Since the system uses renewable energy source, it can be effectively used in a wide range of applications, including the uninterruptible power supply (UPS) system.

Data Availability

The SEPIC data used to support the findings of this study are included within the article.

Conflicts of Interest

The authors declare that they have no conflicts of interest.

Acknowledgments

Theauthors are thankful to the Deanship of Scientific Research at Najran University for funding this work under the Research Groups Funding Program (NU/RG/SERC/11/6).

References

[1] K. Jyotheeswara Reddy and S. Natarajan, "Energy sources and multi-input DC-DC converters used in hybrid electric vehicle applications–A review," *International Journal of Hydrogen Energy*, vol. 43, no. 36, pp. 17387–17408, 2018.

[2] K. T. Chau and C. C. Chan, "Emerging energy-efficient technologies for hybrid electric vehicles," *Proceedings of the IEEE*, vol. 95, no. 4, pp. 821–835, 2007.

[3] C. Thiel, A. Perujo, and A. Mercier, "Cost and CO2 aspects of future vehicle options in Europe under new energy policy scenarios," *Energy Policy*, vol. 38, no. 11, pp. 7142–7151, 2010.

[4] G. Fontaras, T. Grigoratos, D. Savvidis et al., "An experimental evaluation of the methodology proposed for the monitoring and certification of CO2 emissions from heavy-duty vehicles in Europe," *Energy*, vol. 102, pp. 354–364, 2016.

[5] L. Kumar and S. Jain, "Electric propulsion system for electric vehicular technology: a review," *Renewable and Sustainable Energy Reviews*, vol. 29, pp. 924–940, 2014.

[6] A. Mahmoudzadeh Andwari, A. Pesiridis, S. Rajoo, R. Martinez-Botas, and V. Esfahanian, "A review of Battery Electric Vehicle technology and readiness levels," *Renewable and Sustainable Energy Reviews*, vol. 78, pp. 414–430, 2017.

[7] M. Forouzesh, Y. Shen, K. Yari, Y. P. Siwakoti, and F. Blaabjerg, "High-efficiency high step-up DC–DC converter with dual coupled inductors for grid-connected photovoltaic

systems," *IEEE Transactions on Power Electronics*, vol. 33, no. 7, pp. 5967–5982, 2018.

[8] A. Naderi and K. Abbaszadeh, "High step-up DC–DC converter with input current ripple cancellation," *IET Power Electronics*, vol. 9, no. 12, pp. 2394–2403, 2016.

[9] T. K. S. Sathayanarayanan, M. Ramasamy, C. Bharatiraja, and J. L. Munda, "Modelling, impedance design, and efficiency analysis of battery assists PV tied quasi-Z source inverter," *International Journal of Power Electronics and Drive Systems*, vol. 7, no. 3, p. 816, 2016.

[10] M. Vijayakumar and M. Ramasamy, "Performance evaluation of UPQC for interconnecting photovoltaic systems to the electric grid," *Journal of Testing and Evaluation*, vol. 44, no. 4, pp. 20140474–20141616, 2016.

[11] L. Li, S. Coskun, F. Zhang, R. Langari, and J. Xi, "Energy management of hybrid electric vehicle using vehicle lateral dynamic in velocity prediction," *IEEE Transactions on Vehicular Technology*, vol. 68, no. 4, pp. 3279–3293, 2019.

[12] A. Battiston, E. H. Miliani, S. Pierfederici, and F. Meibody-Tabar, "Efficiency improvement of a quasi-Z-source inverter-fed permanent-magnet synchronous machine-based electric vehicle," *IEEE Transactions on Transportation Electrification*, vol. 2, no. 1, pp. 14–23, 2016.

[13] M. Bharathidasan and V. Indragandhi, "Review of power factor correction (PFC) AC/DC-DC power electronic converters for electric vehicle applications IOP conference series: materials science and engineering," *IOP Conference Series: Materials Science and Engineering*, vol. 906, no. 1, Article ID 012006, August, 2020 .

[14] Y. Zheng, W. Xie, and K. M. Smedley, "Interleaved high step-up converter with coupled inductors," *IEEE Transactions on Power Electronics*, vol. 34, no. 7, pp. 6478–6488, 2019.

[15] K. V. Singh, H. O. Bansal, and D. Singh, "A comprehensive review on hybrid electric vehicles: architectures and components," *Journal of Modern Transportation*, vol. 27, no. 2, pp. 77–107, 2019.

[16] A. Kachhwaha, G. I. Rashed, A. R. Garg et al., "Design and performance analysis of hybrid battery and ultracapacitor energy storage system for electrical vehicle active power management," *Sustainability*, vol. 14, no. 2, p. 776, 2022.

[17] L. Kouchachvili, W. Yaïci, and E. Entchev, "Hybrid battery/supercapacitor energy storage system for the electric vehicles," *Journal of Power Sources*, vol. 374, pp. 237–248, 2018.

[18] Z. Song, J. Li, J. Hou, H. Hofmann, M. Ouyang, and J. Du, "The battery-supercapacitor hybrid energy storage system in electric vehicle applications: a case study," *Energy*, vol. 154, pp. 433–441, 2018.

[19] G. Subramanian and J. Peter, "Integrated Li-ion battery and super capacitor based hybrid energy storage system for electric vehicles," in *Proceedings of the 2020 IEEE International Conference on Electronics, Computing and Communication Technologies (CONECCT)*, IEEE, Bangalore, India, July 2020 .

[20] T. Mesbahi, P. Bartholomeüs, N. Rizoug, R. Sadoun, F. Khenfri, and P. L. Moigne, "Advanced model of hybrid energy storage system integrating lithium-ion battery and supercapacitor for electric vehicle applications," *IEEE Transactions on Industrial Electronics*, vol. 68, no. 5, pp. 3962–3972, 2021.

[21] N. A. Dung, P. P. Hieu, Y. C. Hsieh, J. Y. Lin, Y. C. Liu, and H. J. Chiu, "A novel low-loss control strategy for bidirectional DC–DC converter," *International Journal of Circuit Theory and Applications*, vol. 45, no. 11, pp. 1801–1813, 2017.

[22] B. R. Lin and C. W. Chu, "Hybrid DC–DC converter with high efficiency, wide ZVS range, and less output inductance," *International Journal of Circuit Theory and Applications*, vol. 44, no. 5, pp. 996–1011, 2016.

[23] M. Premkumar, C. Kumar, and R. Sowmya, "Analysis and implementation of high-performance DC-DC step-up converter for multilevel boost structure," *Frontiers in Energy Research*, vol. 7, p. 149, 2019.

[24] K. Sayed, A. Almutairi, N. Albagami, O. Alrumayh, A. G. Abo-Khalil, and H. Saleeb, "A review of DC-AC converters for electric vehicle applications," *Energies*, vol. 15, no. 3, p. 1241, 2022.

[25] R. Faraji and H. Farzanehfard, "Soft-switched non-isolated high step-up three-port DC–DC converter for hybrid energy systems," *IEEE Transactions on Power Electronics*, vol. 33, no. 12, pp. 10101–10111, 2018.

[26] S. Salehi Dobakhshari, J. Milimonfared, M. Taheri, and H. Moradisizkoohi, "A quasi-resonant current-fed converter with minimum switching losses," *IEEE Transactions on Power Electronics*, vol. 32, no. 1, pp. 353–362, 2017.

[27] M. Bharathidasan, V. Indragandhi, R. Kuppusamy, Y. Teekaraman, S. Urooj, and N. Alwadi, "Intelligent fuzzy based high gain nonisolated converter for DC microgrids," *Computers, Materials & Continua*, vol. 71, no. 2, pp. 4069–4084, 2022.

[28] R. Gules, W. M. Dos Santos, F. A. Dos Reis, E. F. R. Romaneli, and A. A. Badin, "A modified SEPIC converter with high static gain for renewable applications," *IEEE Transactions on Power Electronics*, vol. 29, no. 11, pp. 5860–5871, 2014.

[29] Y. Hu, R. Zeng, W. Cao, J. Zhang, and S. J. Finney, "Design of a modular, high step-up ratio DC–DC converter for HVDC applications integrating offshore wind power," *IEEE Transactions on Industrial Electronics*, vol. 63, no. 4, pp. 2190–2202, 2016.

[30] E. Babaei, Z. Saadatizadeh, and P. Chavoshipour Heris, "A new topology for non-isolated multiport zero voltage switching dc-dc converter," *International Journal of Circuit Theory and Applications*, vol. 46, no. 6, pp. 1204–1227, 2018.

[31] Z. Saadatizadeh, P. Chavoshipour Heris, E. Babaei, and F. Sadikoglu, "Expandable interleaved high voltage gain boost DC-DC converter with low switching stress," *International Journal of Circuit Theory and Applications*, vol. 47, no. 5, pp. 782–804, 2019.

[32] M. Mahmoudi, A. Ajami, and E. Babaei, "A non-isolated high step up DC -DC converter with integrated 3 winding coupled inductor and reduced switch voltage stress," *International Journal of Circuit Theory and Applications*, vol. 46, no. 10, pp. 1879–1898, 2018.

[33] M. Bharathidasan and V. Indragandhi, "Design and implementations of high step-up non-isolated DC-DC converters for electric vehicles application," *International Journal of Circuit Theory and Applications*, 2022.

[34] Y. P. Siwakoti, A. Mostaan, A. Abdelhakim et al., "High-voltage gain quasi-SEPIC DC–DC converter," *IEEE Journal of Emerging and Selected Topics in Power Electronics*, vol. 7, no. 2, pp. 1243–1257, 2019.

[35] N. Kanagaraj, M. Ramasamy, H. Rezk, and T. Manesh, "Modified bidirectional DC-DC Boost converter fed three-phase four-wire PV-DVR," *Journal of Testing and Evaluation*, vol. 48, no. 4, pp. 20180111–20183115, 2018.